Journal of Alloys and Compounds 936 (2023) 168298

Contents lists available at ScienceDirect

Journal of Alloys and Compounds

journal homepage: www.elsevier.com/locate/jalcom

Ultrasonically assisted hot-wire arc additive manufacturing process of AA7075 metal matrix nanocomposite

Tianzhao Wang *, Jiarui Kang, Mason Darnell, Xun Liu *

Welding Engineering Program, Department of Materials Science and Engineering, The Ohio State University, 1248 Arthur Adams Drive, Columbus, OH 43221, United States

ARTICLE INFO

Article history:
Received 10 September 2022
Received in revised form 18 November 2022
Accepted 29 November 2022
Available online 30 November 2022

Keywords:
Wire arc additive manufacturing
Power ultrasound
Metal matrix nanocomposite
Hot-wire GTAW

ABSTRACT

A newly developed ultrasonically assisted (UA) hot-wire wire arc additive manufacturing (HWAAM) process for TiB_2 nanoparticle reinforced AA7075 metal matrix nanocomposite (MMNC) was thoroughly studied. The synergic effects of UA and hot-wire system were discussed along with process parameters. HWAAM samples showed reduced porosities and improved deposition rate compared to conventional WAAM, while UA-HWAAM further upgraded the process and showed improvements in several aspects: reduced porosities, better dispersion of nanoparticles, and uniform microstructure, as reflected in the more homogeneous hardness distribution, and enhanced mechanical properties. Lower travel speed shows more significant UA improvements based on the longer UA-melt interaction time.

© 2022 Elsevier B.V. All rights reserved.

1. Introduction

Aluminum based metal matrix nanocomposite (MMNC) has been widely used in various industries due to its promising properties for different applications: outstanding specific strength, excellent high temperature properties, and sound ductility[1]. Nanoparticles are utilized in AA7075 alloy to reduce solidification cracking and make it applicable for welding [2] and laser additive manufacturing processes [3]. The nano-sized reinforcement contribute to the weldability and material mechanical properties by several mechanisms [4–6]. First, nanoparticles add to the heterogeneous nucleation sites during solidification. In the meanwhile, nanoparticles decelerate the solidification front and increase the amount of undercooling at the solid-liquid (S-L) interface [2]. These help formation of refined equiaxed grains instead of large columnar dendritic structure, which avoid stress concentration at the flat centerline of the ends of columnar dendrites to reduce solidification cracking. Refined grains also directly enhance boundary strengthening in MMNC. Second, Orowan strengthening of nanoparticles greatly increases the strength of MMNC. During plastic deformation, dislocations get pinned at or bow around nanoparticles. Well dispersed nanoparticles with fine interspacing could increase the strength for up to 76.6% from theoretical calculations [5].

Despite all the merits from nano-sized reinforcements, several challenges are associated with MMNC fabrication. Nanoparticles are highly susceptible to agglomeration during solidification. Clustered nanoparticles can drastically reduce the ductility of MMNC [7] as large clusters cause stress concentration. Besides, the Orowan strengthening effects are diminished as the particle interspace is increased with agglomerations and the strength is inversely proportional to interspace distance. For clusters with the size of over 5 μm, Orowan strengthening will be minimal [8]. Besides, non-metallic particles can serve as hydrogen concentrators and lead to porosities issues [9,10]. According to the synchrotron radiographic imaging analysis in [11], a significant increase in numbers of hydrogen bubbles is induced by Al_2O_3 nanoparticles in the melt of Al-10 wt% Cu alloy system.

As a rapid prototyping process, wire arc additive manufacturing (WAAM) provides near-net-shape products with high deposition rates [12]. However, WAAM of MMNC is still subject to porosity issues and nanoparticle agglomerations due to the inherent solidification behavior. To address these concerns, ultrasonic energy has been applied for degassing in conventional molten metal processing based on acoustic cavitation and streaming effects [9,13]. Besides, ultrasonic energy is also applied for better nanoparticle dispersion during fabrication of MMNC [14]. In terms of ultrasonically assisted (UA) additive manufacturing (AM), several different approaches showed decent enhancements from UA. In [15], an ultrasonic forging head was placed behind the molten pool during laser wire AM, which produced refined equiaxed grains and less porosities. In [16],

* Corresponding authors.
E-mail addresses: wang.13522@osu.edu (T. Wang), liu.7054@osu.edu (X. Liu).

https://doi.org/10.1016/j.jallcom.2022.168298
0925-8388/© 2022 Elsevier B.V. All rights reserved.

ultrasonic vibration was supplied through the substrate during laser powder-based AM and showed a full microstructure transition from columnar to equiaxed grains. Despite the promising UA enhancement, this configuration leads to UA energy attenuation during transmission with varying amplitudes at different locations, which may cause inhomogeneity in the deposition and a low UA energy efficiency. In our previous works in [17], the UA probe was directly immersed into the weld pool following the arc in a gas tungsten arc-based (GTA) WAAM process, which promoted a more uniform microstructure and enhanced mechanical properties for TiB_2 based AA7075 MMNC. However, porosities and low deposition rate remained as main concerns.

Hot-wire system has been commonly applied in gas tungsten arc welding for higher deposition rate by resistance heating of the weld wires [18]. Hot-wire system was also applied in GTA-WAAM of aluminum alloys and showed reduction of porosities [19]. It was explained that hot-wire heating cleaned the wire surface and modified the behavior of hydrogen in the melt during the process. So far, combination of UA and hot-wire GTA-WAAM has not been investigated. In this study, the UA-WAAM setup in [17] was upgraded by integrating the hot-wire system. The ultrasonically assisted hot-wire arc additive manufacturing (UA-HWAAM) process was studied on TiB_2 nanoparticle reinforced AA7075 MMNC. The interaction mechanisms between UA and hot-wire system were analyzed.

2. Materials and experimental methods

2.1. Materials

TiB_2 nanoparticles enhanced AA7075 weld wires (AA7075NT, MetaLi LLC) with a diameter of 1.2 mm were used for the deposition process. The nano-treated weld wires were manufactured via a flux assisted liquid state incorporation method followed by hot extrusion and 1.7 vol% TiB_2 nano-reinforcements were added with an ideal size of 40–60 nm in diameter [2]. TiB_2 nanoparticles have high thermal stability (melting point of 2790 °C) and hardness (960HV), and will not react with molten aluminum matrix [20]. An AA7075 base plate with a thickness of ¾ inches was served as the substrate for the deposition.

2.2. Ultrasonic assisted hot-wire arc additive manufacturing (UA-HWAAM) system

Fig. 1 shows the schematic diagram of the UA-HWAAM system, which is adapted from the UA-WAAM setup in [17]. A non-consumable tungsten electrode is applied for the welding arc, with the filler metal being fed in front of the arc and the UA probe traveling behind. Argon shielding gas is applied at a flow rate of 9.5 L/min

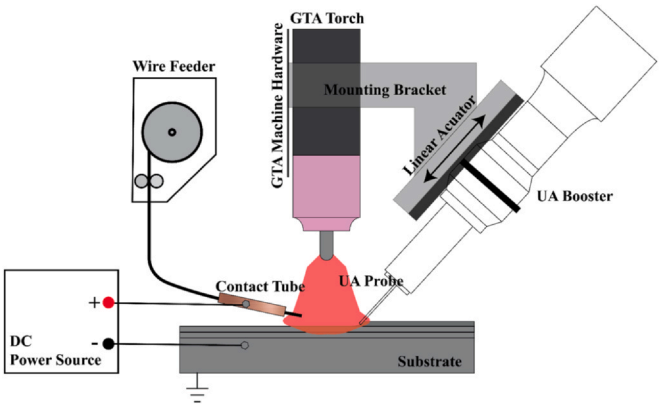

Fig. 1. Schematic illustration of UA-HWAAM setup.

throughout the entire building process. Resistance heating of the welding wire is provided with a DC power supply. Wire feeder is connected to the positive output and the deposition substrate is grounded. Heat input of the hot-wire system is adjusted by the voltage of the DC power supply. Based on initial investigations, inadequate voltage would cause clogged wires while excessively high voltage would interfere with the welding arc. A 4 V voltage was selected for optimized process window of other deposition parameters.

2.3. UA-HWAAM process parameters

Table 1 summarized the process parameters of the UA-HWAAM process. Two groups of experiments with different travel speeds were performed to study how different travel speeds and energy densities affect the effectiveness of UA. Samples are designated based on the process parameters, where the first letter is the group number, second digit represents the travel speed, and the last digit is the UA power percentage. Group #A was performed at the travel speed of 3 in./min (IPM) while Group #B was running at a lower travel speed of 2 IPM for a higher energy density and longer interaction time of UA and the melt. Moreover, different UA power percentages were assigned in Group #A tests to further reveal the optimized UA amplitude for current process, which was applied in Group #B tests afterwards. UA power percentages of 30% and 60% corresponded to a peak-to-peak vibration amplitude of 10.7 µm and 20.7 µm respectively. No-UA represented conventional GTA-WAAM deposition process without introducing UA probe into the melt pool. Furthermore, since the UA probe itself could cause heat dissipation from the local melt, a second control test was carried out with only UA probe inserted in the weld pool without any vibration (designated as X for the third digit). During the process, the tip of the UA probe was adjusted to the same height as the melt surface and its horizontal distance to the arc center was 2.5 mm.

For each parameter combination, 5 passes of deposition were performed. For a better understanding of the energy and material input comparison, heat input Q(kJ/inch), deposition rate R(10^{-3}lb/inch), and energy density μ(MJ/lb) were calculated as:

$$Q = \frac{V \cdot I}{v} \tag{1}$$

$$R = \frac{\rho \cdot \pi \cdot r^2 \cdot w}{v} \tag{2}$$

$$\mu = \frac{\eta_m \cdot Q}{R} + q_{HW} \tag{3}$$

where V is the voltage, I is the current, v stands for the travel speed, ρ is the density of the weld wire, r is the radius of the weld wire, w is the wire feed speed, and η_m is the melting efficiency of the process. The melting efficiency η_m describes the percentage of heat input consumed for melting the wire compared with the total arc energy input Q per unit length. The η_m is set at 10% by comparing travel speed and current in this study with literature range [21]. Heat input of hot-wire system is designated as q_{HW}, which is calculated based on the average voltage and current of the DC power supply (4 V and 50 A). The deposition rate R is the weight of material deposited per unit length during the process. Energy density μ represents the amount of energy input on the weld wire per unit mass.

An AC pulse waveform with a frequency of 70 Hz and 50% of electrode positive (EP%) is applied during the deposition. As material is deposited to the substrate at higher layers, the heat conduction through the bottom reduces while heat convection and radiation to the surrounding atmosphere increases, which is less effective in heat dissipation. Accordingly with the same heat input, the deposition layer at higher building height tends to get over-heated and lose dimensional control [12]. Thus, heat input is decreased for each pass

Table 1
Process parameters of UA-HWAAM process.

Group	Designation	UA Status	Pass No.	Voltage/ V (V)	Current/ I (A)	Travel Speed/ v (inches/min)	Feed Speed/ w (inches/min)	Heat Input/ Q (kJ/inch)	Deposition Rate/ R (10^{-3}lb/inch)	Energy Density/ μ (MJ/lb)
#A	A30	no-UA	1	13.5	330	3	45	89.10	2.67	4.840
	A33	30% UA	2		285			76.95		3.385
	A36	60%UA	3		265			71.55		4.183
			4		215			58.05		3.676
			5		200			54.00		3.525
#B	B20	no-UA	1	13.5	330	2	40	133.65	3.56	5.458
	B23	30% UA	2		285			115.43		4.946
	B2X	Probe-only	3		265			107.33		4.718
			4		215			87.08		4.148
			5		200			81.00		3.978

to avoid excessive heat accumulation in all the deposits, as shown in Table 1. To maintain a stable arc length, the voltage remains constant while the current is reduced.

2.4. Thermal imaging of the weld pool

Temperature distribution was obtained via an infrared (IR) camera (FLIR IR) at a frame rate of 40 Hz and a resolution of 320 × 256. A neutral density filter was placed within the camera lens and calibrated to capture thermal information at the temperature range of 487–2000 °C. The temperature distribution of the melt pool top surface during the 3rd deposition pass was captured from the side view at travel speed conditions of 3ipm and 2ipm. The mean temperature of the center melt pool was calculated based on the IR images.

2.5. Mechanical and microstructure characterization

Metallurgical samples were sectioned perpendicular to deposition direction, which were then ground and polished according to standard metallurgical procedures. Vickers micro-hardness mapping was carried out on the polished cross-sections of the build samples at a load of 100 g with an interspacing distance of 150 μm. The micro-hardness of the weld wire was also measured as a baseline comparison.

Micro tensile specimens were extracted from B20 and B23 samples along the vertical deposition direction with a gauge length of 1.5 mm, gauge width of 0.36 mm and thickness of 0.15 mm, as shown in Fig. 2(b). Side view and 45° angled view of the builds with and without UA were shown in Fig. 2(a). As shown in Fig. 2(a) and (b), micro-tensile specimens covered the interlayer region. Tensile tests at a strain rate of 0.06/s were performed on a customized micro-tensile testing system adapted from Kang et al. [24]. At least five specimens were tested in each build. 2D digital image correlation (DIC) analysis was performed during the micro-tensile tests to reveal evolution of the strain distribution. This was achieved with high-speed photography of the speckle patterned tensile bars at a frame rate of 250 fps. Strain distribution was calculated by tracking subsets of the images during loading, setting the image of initial stage as the reference.

Polished cross-section samples were etched with Keller's reagent to reveal grain boundaries. Grain size distribution and grain morphology were analyzed with the Mipar image processing software, by thresholding image color to identify grain boundaries. Scanning electron microscope (SEM) equipped with Energy-dispersive X-ray spectroscopy (EDS) detector was employed to analyze the distribution of TiB_2 nanoparticles, secondary phases, and precipitates. EDS was performed with a counting rate of 40k counts/sec. To further study the formation of nanoparticle clusters in the build, weld wire microstructure was also characterized with SEM.

3. Results and discussion

3.1. Molten pool temperature distribution

Fig. 3 showed the temperature distribution of the molten pool during the 3rd pass of HWAAM process at different travel speeds without ultrasound, corresponding to A20 and B20 samples. Overall, a higher temperature distribution was observed at the lower travel speed of 2IPM condition, indicating a hotter and larger weld pool.

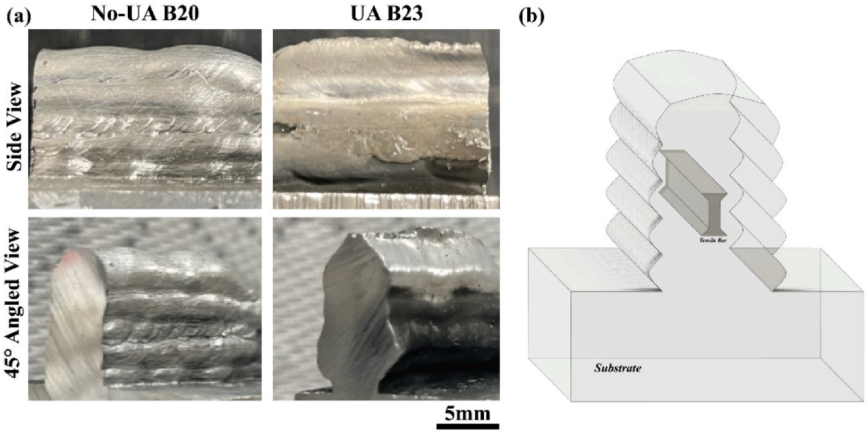

Fig. 2. (a) Photos showing the side and 45° angled view of the builds B20 without UA and B23 with UA; (b)Schematic of micro tensile bar extraction.

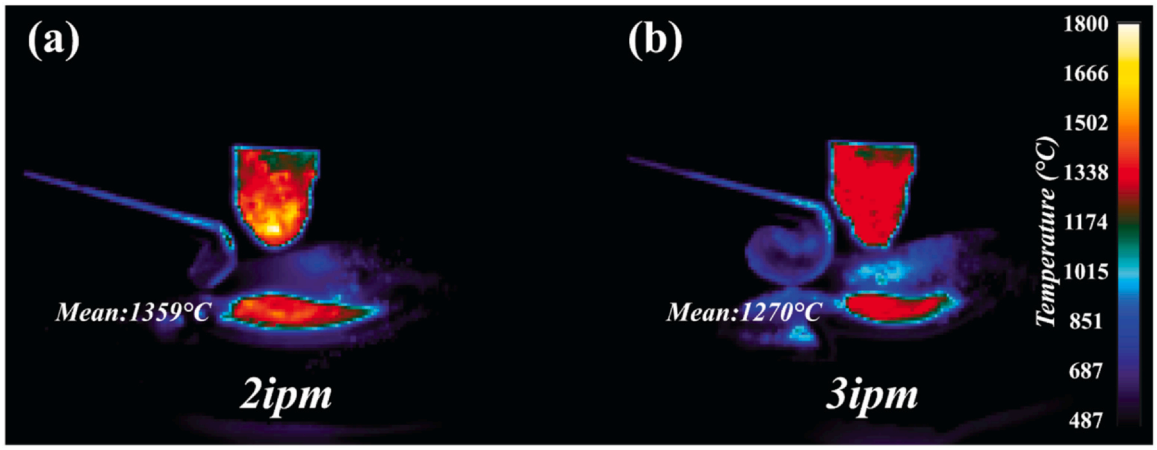

Fig. 3. Temperature distribution of the melt pool top surface from the side view at the travel speed of (a) 2ipm and (b) 3ipm.

The average temperature of the center molten pool was calculated for further comparison. The 2IPM case showed a center molten pool temperature of around 1359 °C, while that in 3IPM case was around 1270 °C. This was in accordance with the higher energy input at lower travel speed, as shown in Table 1.

3.2. Deposition geometry

Fig. 4 showed the macrostructure of the cross-section of all samples. Comparing with the samples fabricated by WAAM and UA-WAAM processes in [17], the amount of porosities were remarkably

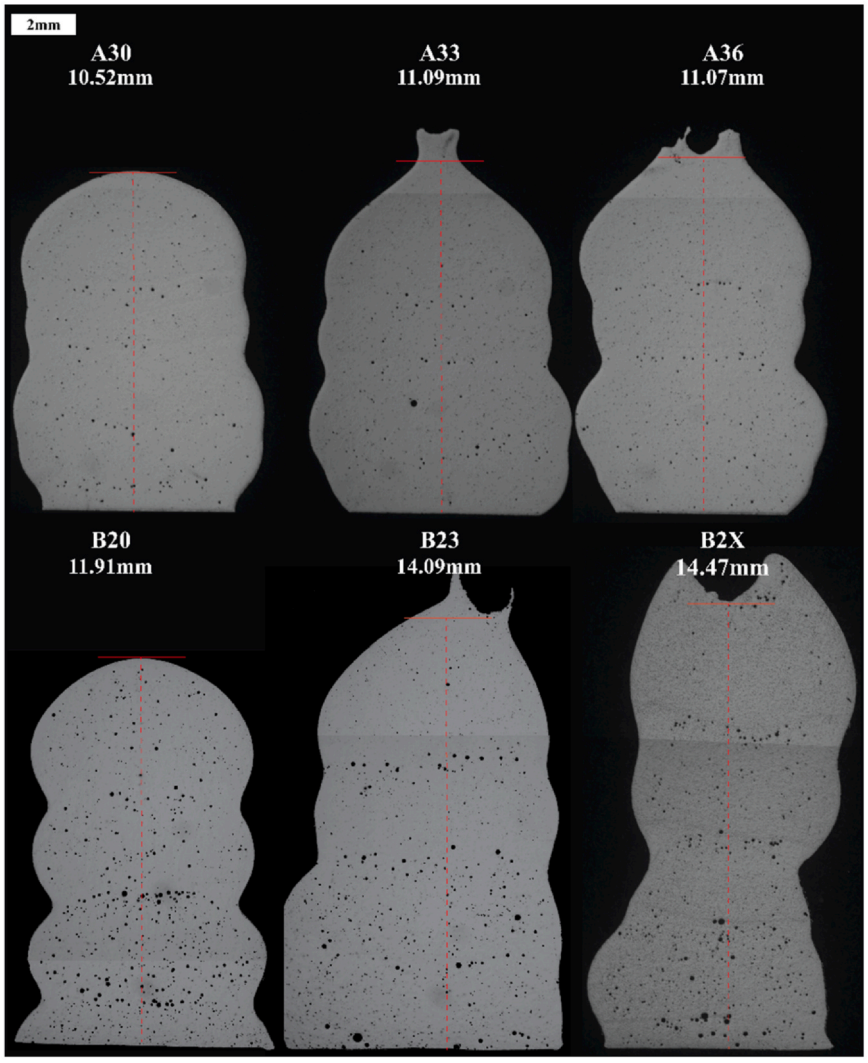

Fig. 4. Macroscopical images of cross-sections in all the investigated deposition conditions. Total building height was measured and provided on the top of each sample.

reduced in both conditions, which could be attributed to the hot wire system. Furthermore, the building height per pass was increased. In A30 of 5 passes, the height was 10.52 mm. In the previous study without the hot-wire system [17], 20 passes of deposition only led to a building height of 16.8 mm. In conventional GTA-WAAM, the feedstock was heated up from the room temperature and melted by the heat input only from the arc. Thus, the material feeding rate was limited to the melt efficiency of the system. Hot-wire system provided extra resistance heat input into the wire, which preheated the wire and allowed more material to be melted by the arc, and accordingly increased the deposition rate.

All UA samples, including the one with UA probe in but no vibration (B2X), showed a steeple-roof feature at the very top layer. This was caused by the intermolecular adhesive forces between the UA probe and the melt, which propagated along the molten pool and further constrained the melt from falling to the sides. The total building height was measured based on the effective height (indicated by red dashed lines in Fig. 4). Samples in the Group #B showed a higher building height than the corresponding Group #A ones, which was mainly due to the higher material deposition rate from low travel speed and the similar wire feed speed, as calculated in Table 1. Samples built with UA probe in, including the B2X, all presented higher height than corresponding conventional ones. Comparing A33 with A36 samples, changing UA vibration amplitude showed minimal effect on the deposition height. B23 with 30% UA energy input also showed similar building height as the control sample B2X, where the UA probe was in the molten pool without vibration. However, a large surface scratch was observed in the B2X sample. This indicated that only the UA probe itself could also increase the building height by the adhesive force between the probe and melt. However, the build quality significantly deteriorated without UA energy input. The building height difference between UA and no-UA sample was larger in Group #B than Group #A. This could be explained by the more interaction time between the UA probe and the melt pool, which was a result of lower travel speed and larger melt pool in Group #B.

3.3. Hydrogen dynamic in the weld pool of UA-HWAAM process

Hydrogen porosities have been one of the major issues with aluminum welding process, where the hydrogen can come from moisture, grease, and surface contaminations [19]. Porosities were significantly reduced in the UA-HWAAM process compared with the previous UA-WAAM study [17] for the same material. The majority fraction of porosities was observed at the interlayer regions in all samples. Group #A performed at a higher welding speed showed a lower number of porosities than Group #B. Regarding the UA effect, UA samples in the Group #A (A33&A36) showed slightly less porosity than the no-UA sample A30. Higher UA intensity sample A36 showed similar porosity distribution as the lower UA case A33. In comparison, the B23 presented a clearly reduced porosity distribution than the no-UA B20 sample, indicating the UA effect was more significant under a lower welding speed. This could be attributed to the longer interaction time between the UA probe and the molten pool. The control test B2X showed the highest number of macropores among all conditions, which meant the insertion of a non-vibrating probe in the melt pool would introduce contaminates and greatly degraded the solidification structure.

The hydrogen behavior during solidification consists of nucleation, growth, detachment, and escape stages. Deposition process parameters, UA, and hot-wire all modified these stages and resulted in a different porosity distribution.

3.3.1. Nucleation of hydrogen bubbles

K. Li et al. [22] and Poirier et al. [23] proposed an analytical solution to the nucleation of hydrogen porosity during solidification of molten aluminum: hydrogen gas bubbles nucleate when the pressure of the gas phase P_{H_2} exceeds the surrounding local pressure of molten metal P_l and the pressure $P_\sigma$induced by the surface tension. The hydrogen gas pressure P_{H_2} can be determined by the concentration of hydrogen at the solid/liquid (S/L) interface based on Sievert's law. The mathematical expression of nucleation criterion is the following:

$$P_{H_2} = (C_l/K)^2 \geq P_l + P_\sigma \tag{4}$$

where $C_l$stands for the concentration of hydrogen in liquid and K is the Sievert's constant of hydrogen ($0.8\mu mol/g{\cdot}Pa^{0.5}$). The local pressure of molten aluminum P_l is approximated as 1 atm. By assuming hydrogen nucleates as a perfect spherical bubble in 2D, the surface tension pressure P_σ can be calculated via Laplace's law [24]:

$$P_\sigma = \frac{2\sigma}{r} \tag{5}$$

where σ is the surface tension between gas and liquid, and r is the radius of the gas bubbles (assumed as 20 μm based on the averaged experimental measurement in this study). The surface tension was set as a constant of 0.8 N/m adapted from reference [25]. The threshold pressure was calculated as 1.8 atm via equation (4) and (5).

Hydrogen can potentially segregate at the S-L interface during rapid-cooling process [22], which result in an elevation of local hydrogen concentration and form hydrogen bubble nuclei. The local segregated hydrogen concentration at the S-L interface can be calculated as[26]:

$$C_l = C_0\left\{1 + \frac{1-k}{k}\exp\left(-\frac{R}{D}x\right)\right\} \tag{6}$$

where C_0 is the initial hydrogen concentration in the aluminum melt at the beginning of the solidification, k is the partition coefficient of hydrogen in aluminum, R is the growing velocity of solid grain, D is the diffusivity of hydrogen in the liquid aluminum, and x is the distance from the S-L interface. This solution assumes zero convection in the melt, which is different from Scheil's equation. To solve equation (6), k value was set as 0.069 based on reference[23]. D was calculated following the equation in the reference [22], where the temperature was assigned as the solidus temperature of AA7075. R was approximated by the travel speed resolved in the solidification direction with an angle of 45°. C_0 is determined as the solubility of hydrogen at temperatures of the melt during the deposition process [27]:

$$\log\frac{C_0}{C_{ref}} = \frac{-2700}{T + 273.15} + 2.72 \tag{7}$$

where C_{ref} is a reference composition of hydrogen of 1 $cm^3/100$ g, and T here is the center molten pool temperature in °C during WAAM process, which is determined from the measured thermal imaging data as presented in Fig. 3. Since the temperature of the molten pool during WAAM is much higher than the aluminum liquidus temperature, at the beginning of solidification, the aluminum melt will be supersaturated with hydrogen. The calculated C_0 is 2.90 $cm^3/100$ g at the travel speed of 2IPM and 2.63 $cm^3/100$ g at 3IPM. By plugging in C_0 value into equation (5), the hydrogen concentration profile can be calculated and further converted into hydrogen pressure based on Sievert's law at the S-L interface. The results were plotted in Fig. 5(a) and compared with the threshold nucleation pressure. At both 2IPM and 3IPM travel speeds, the hydrogen concentration at the S-L interface was sufficient for bubble nucleation. Away from the S-L interface, the lower travel speed 2IPM enabled bubble nucleation at a further distance, which indicated higher amount of porosity nucleation.

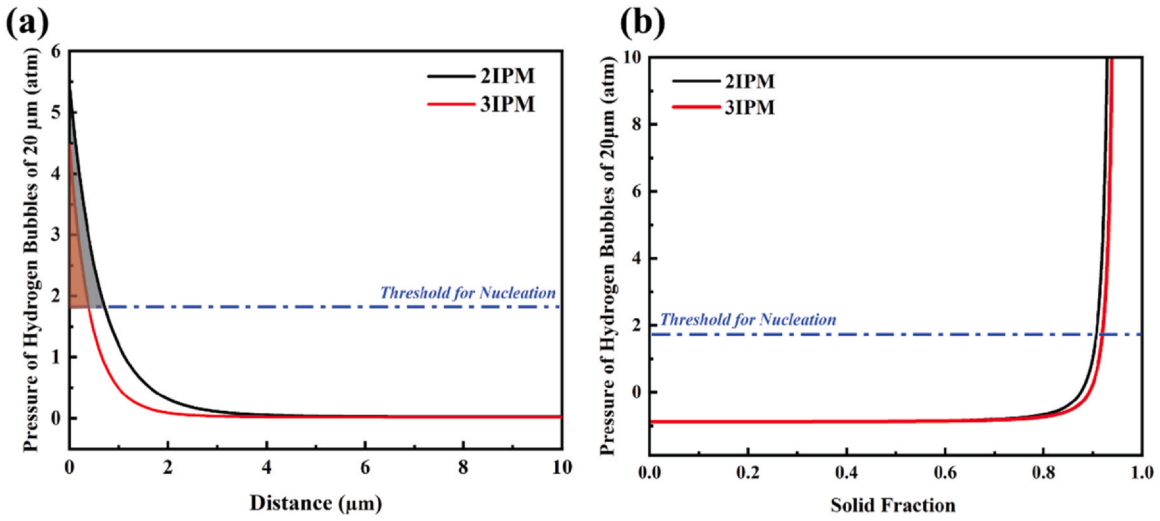

Fig. 5. Calculated pressure of hydrogen bubbles with a diameter of 20 μm based on (a) segregation of hydrogen near the S-L interface and (b) Scheil's analysis with solute trap during the solidification process.

On the other hand, during WAAM, multiple driving forces effectively enhance the convective fluid flow in the molten pool, including arc pressure, Marangoni force, and electromagnetic forces [28]. A plasma jet, i.e. the arc, forms between the workpiece and the electrode and the plasma inherently generates a strong electromagnetic field around itself. Due to the electromagnetic force, the plasma thrusts downward along the vertical direction and therefore applies an arc pressure on the molten pool surface, which affects the molten pool shape and drives fluid flow in the molten pool. The melt in the molten pool also reacts to the electromagnetic field and flows along the field line. Meanwhile, the molten pool during the GTAW process has a temperature gradient, which induces a gradient of surface tension in the molten pool since the surface tension is a function of temperature. Liquid with higher surface tension pulls more effectively against the lower surface tension liquid and causes extra fluid flow. In this case, the surface tension of aluminum usually has an inversely proportional relationship against temperature. Thus, the molten pool center with lower surface tension yields to the higher tension melt around and forms an outward fluid flow. Adding up these driving forces, the flow velocity in the molten pool can be up to 0.8 m/s in arc welding [29]. Furthermore, the UA vibration additionally drives the hydrodynamic flow, known as the acoustic streaming, which promotes the circulation of the liquidus and enhances mixing of solutes [30]. Besides, UA induced sinusoidal pressure field in the melt drives the formation, growth, and implosive collapse of the cavitation bubbles, known as the acoustic cavitation effect [9]. The collapse of hydrogen cavitation bubbles will generate shockwaves, which induce secondary streaming to further facilitate the mixing of solutes in the liquid. Thus, the UA along with intrinsic driving forces of arc welding diminish the segregation of hydrogen, which reduces the nucleation tendency. The analysis in Fig. 5(a) conceptionally outlines the effect of travel speed upon local hydrogen concentration in the melt, but only partially represents the behavior of hydrogen during the process.

Accordingly, the segregation behavior of hydrogen at the S/L interface should be closer to the Scheil's non-equilibrium solidification analysis, which assumes infinite mixing of solutes in the liquid [31]. On the other hand, since additive manufacturing is generally considered as a rapid solidification process, the liquidus of aluminum is dynamic depending on the solidification rate considering the solute drag effect. To account for this, the Scheil's analysis modified with solute trap is adopted in this study. The hydrogen concentration profile in molten aluminum can be obtained by [32]:

$$C_l(1-k)df_s = (1-f_s)dC_l \tag{8}$$

$$C_l = C_0 at f_s = 0,\ k = f(R)$$

where k is the dynamic partition coefficient of hydrogen in aluminum, which is a function of solidification rate R considering the dynamic liquidus temperature, and f_s stands for the solid fraction.

By solving equation (8) with different travel speeds and temperatures captured by thermal imaging (Fig. 3) using the Thermo-calc software, hydrogen concentration profile can be calculated as a function of solid fraction, which is further converted to hydrogen pressure and presented in Fig. 5(b). Nucleation in both 2IPM and 3IPM occurred at the end of the solidification, which would tend to promote inter-dendritic nucleation [19]. The lower travel speed of 2IPM showed earlier nucleation of hydrogen bubbles, which agreed with experimental results in Fig. 4 and was also consistent with simulation results in Fig. 5(a). It is noteworthy that during the actual WAAM process, the hydrogen nucleation behavior should be in between Fig. 5(a) and Fig. 5(b).

Based on the analytical analysis above, it can be noted that the initial supersaturated hydrogen concentration C_0 is a major factor affecting the nucleation of hydrogen. As shown in Fig. 4, the Group #A samples contain less porosities than corresponding Group #B samples. The Group #A samples were fabricated at a higher travel speed of 3IPM and a lower energy density, which led to a lower molten pool temperature, as shown in Fig. 3. Accordingly, less hydrogen was dissolved from the environment for hydrogen segregation at the S/L interface, which reduced hydrogen bubble nucleation in the Group #B samples. The hydrogen nucleation stage will also be affected by the hot-wire system. Resistance heating of wires before entering molten pool can effectively remove surface contamination, which is one of the major sources of hydrogen [19]. Besides, for the same material deposition rate, less heat input is required from the arc since the wire is melted by both the arc energy and external resistance heating. An average current of 340 A was required in the previous study without the hot-wire system, while an average of 260 A was applied in this set of experiments. Hence, a colder weld pool was obtained with the hot-wire system, which reduced the initial supersaturated hydrogen concentration C_0. Lastly, UA can

interact with nanoparticles on bubble nucleation. It was shown with synchrotron analysis that nanoparticles will enhance the ultrasonic cavitation potential. On one hand, this can help with degassing that reduces porosity. On the other hand, over amount of cavitation bubbles would severely increase the melt agitation, which increases the porosity. This partially explains that the amount of porosity is similar in the low and high UA intensity sample A33 and A36.

3.3.2. Growth of hydrogen bubbles

In the growth stage of hydrogen bubbles, UA can be the dictating factor based on acoustic cavitation effect compared with hot-wire and process parameters. The UA acoustic wave propagates as an oscillating pressure field in the molten aluminum with alternating rarefaction and compression phases [33]. Compression phases impose positive pressure in addition to ambient liquid pressure P_l, while rarefaction phases impose negative pressure. As negative pressure cannot exist in gaseous state, dissolved hydrogen will be forced to emerge out from the molten aluminum. The pulsating cavitations under UA will lead to a distinctive rectified diffusion of hydrogen into the gas bubbles, as described by G.I. Eskin [9]. The one direction motion of hydrogen is the superimposed result of stronger inward diffusion into the gas bubbles in rarefaction and less outward diffusion in compression. In the rarefaction phase of the pulsation cycles, larger surface area in the expanded bubbles accommodate more hydrogen diffusion into the gas bubbles. Moreover, expansion will reduce the thickness of the layer surrounding the cavitation bubbles. The concentration gradient becomes steeper and further enhances the hydrogen diffusion into the bubbles for bubble growth.

3.3.3. Detach and escape of the hydrogen bubbles

Detachment of hydrogen bubbles from the S-L interface can be evaluated by the infiltration angle θ between the bubbles and the solid interface. It follows[19,34]:

$$\cos\theta = \frac{\sigma_{S/G} - \sigma_{S/L}}{\sigma_{L/G}} \tag{9}$$

where $\sigma_{S/G}$ is the surface tension between solid and the gas pore, $\sigma_{S/L}$ is the surface tension between solid and liquid, and $\sigma_{L/G}$ is the surface tension between liquid and gas pores. Detachment is promoted at a smaller infiltration angle. As the temperature of molten aluminum increases, the surface tension terms $\sigma_{S/L}$ and$\sigma_{L/G}$ will decrease [19]. The $\sigma_{S/G}$ remains roughly unchanged, which is controlled by the temperature of the solidification front. Accordingly, an increase in the molten pool temperature decreases the infiltration angle and promotes detachment of gas bubbles.

After the gas bubbles detachment, they float to the melt surface to escape. The escape speed of hydrogen bubbles can be estimated as [35]:

$$v = \frac{2}{9}\frac{(\rho_1 - \rho_2)gr^2}{\eta} \tag{10}$$

where v is the escape speed, ρ_1 is the density of the melt, ρ_2 is the density of hydrogen gas, g is gravitational acceleration, r is the radius of the hydrogen bubble. η is the melt viscosity, which is a function of the melt temperature [36]. Porosity will not form if the bubble escape speed exceeds the solidification rate. Some emerging bubbles get trapped by the solidification front and accumulate around the interlayer due to the relatively high cooling and solidification rate at that region. The concentrated porosity distribution at interlayer can be observed in Fig. 4, which is also commonly reported in WAAM structures [37,38]. On the other hand, reducing the molten pool temperature will increase the melt viscosity, which leads to a lower escape speed. Considering the effects of travel speed, a higher travel speed increases solidification rate and reduces melt temperature, both of which are adverse for bubble escape and can increase porosity level. The reduced melt pool temperature also restrains bubble detachment, both of which indicate increasing the travel speed should increase porosity level. However, the higher travel speed reduced the level of hydrogen bubbles nucleation as discussed in 3.2.1. These competing mechanisms between nucleation and escape overall lead to less porosities under high travel speed as experimentally observed, which indicates that the nucleation is a more dominating factor in this case.

UA induced acoustic streaming and collapse of cavitation bubbles can sweep the solidification front and mobilized hydrogen bubbles in the melt, as was shown in an in-situ X-ray radiography analysis on aluminum alloy solidification [30]. Accordingly, the UA induced hydrodynamic flows can facilitate detachment and escape of hydrogen bubbles. Moreover, acoustic cavitation promoted growth of the hydrogen bubbles, which resulted in a larger bubble radius and faster escaping.

3.4. Microstructure and dispersion of nanoparticles

Different from columnar dendrites of GTAW-based WAAM of conventional aluminum alloys [39], nanoparticles greatly promoted the development of equiaxed solidification structure, as shown in all the samples in this study. Fig. 6 compares the grain size distribution of no-UA and UA samples in the low travel speed Group #B. The two main regions that show clear difference in grain size are marked in blue as position 1 and 3 in Fig. 6(a). These are located at the interlayer regions as shown in Fig. 6(b), which are subject to significant grain growth in the B20 sample without UA. In comparison, the UA B23 sample shows a more uniform grain size distribution as in Fig. 6(c). Between position 1 and position 3, the grain sizes are similar in UA and no-UA samples.

The grain structure at the three positions under different deposition conditions are more thoroughly examined in Fig. 7, where different grains are colored by grain size. No cracking was observed in any of the build samples, which is in contrast to welding of AA7075 [40]. According to M. Sokoluk et al. [2], the reinforcement TiB_2 nanoparticles suppress the growth of AA7075 dendrite arms and act as heterogeneous nucleation sites, which further enhance grain refinement. Moreover, TiB_2 lowers the grain coherency point (GCP) and inhibits early grain connections, leaving more liquid fraction at the terminal stage of solidification. Accordingly, the strength build-up among the solid shell network in the mushy zone is delayed and the brittle temperature range (BTR) is reduced. In addition to the equiaxed solidification structure, more straight grain boundary morphologies are observed at the lower deposition heights in all the samples, which can be related to grain boundary migration due to the reheating cycles during higher layer depositions.

Comparing the effects of deposition parameters, the Group #A samples generally showed a more refined grain structure in all positions than the corresponding ones in Group #B, which could be attributed to the lower molten pool temperature and faster solidification rate associated with higher welding speed. UA samples in Group #A showed greatly refined grain structure in positions 1 and 3 compared with no-UA condition, while minimal difference was observed in Pos. 2. This can be explained by the UA modified thermal history and improved nanoparticle dispersion. According to the thermal imaging in previous study [17], the UA probe introduced an additional heat sink to the weld pool, which dissipated the heat and hence ameliorated the reheating effect. Microstructure analysis in the next session shows that UA will reduce nanoparticle agglomeration, which can restrict the grain growth by boundary pinning effects with better dispersed nanoparticles. On the other hand, increasing the ultrasonic intensity from A33 to A36 did not further reduce the grain size. The higher ultrasonic intensity might have introduced excessive melt flow and cavitation considering the

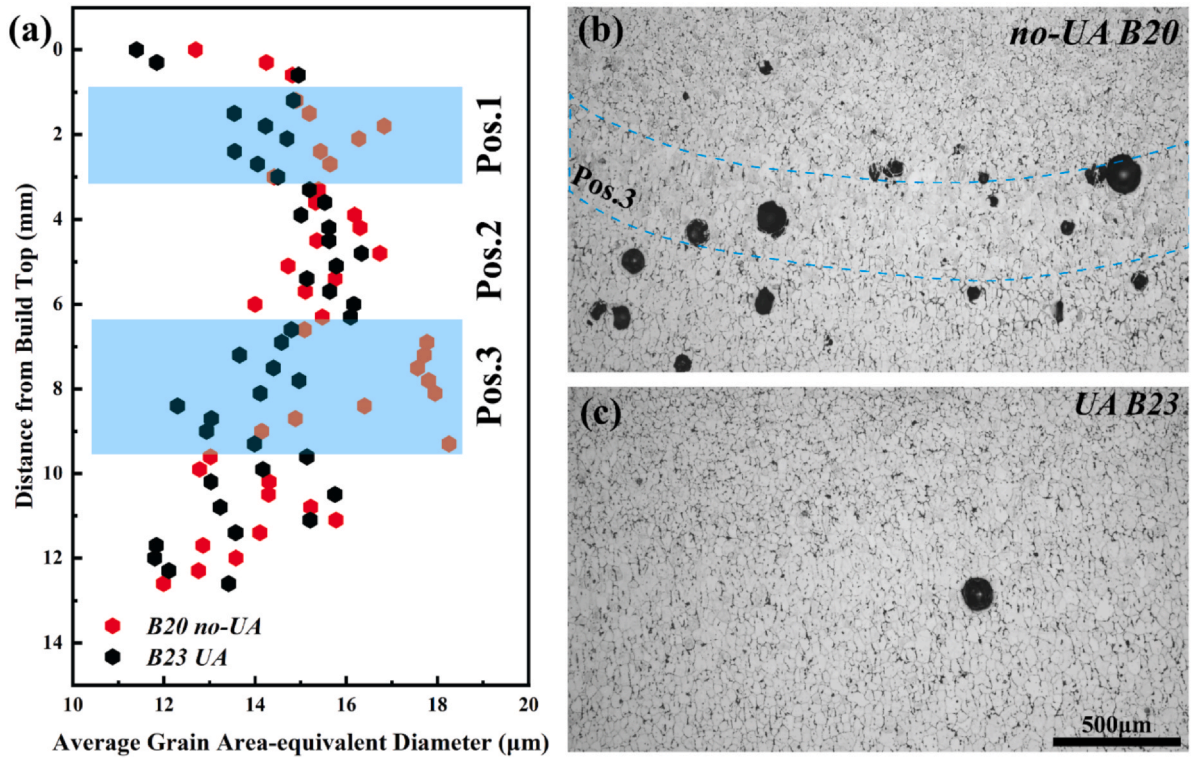

Fig. 6. (a) Grain size distribution of no-UA B20 and UA B23 samples; (b) Optical micrographs show the Position 3 interlayer region in no-UA B20; (c) Position 3 interlayer region in UA B23 samples.

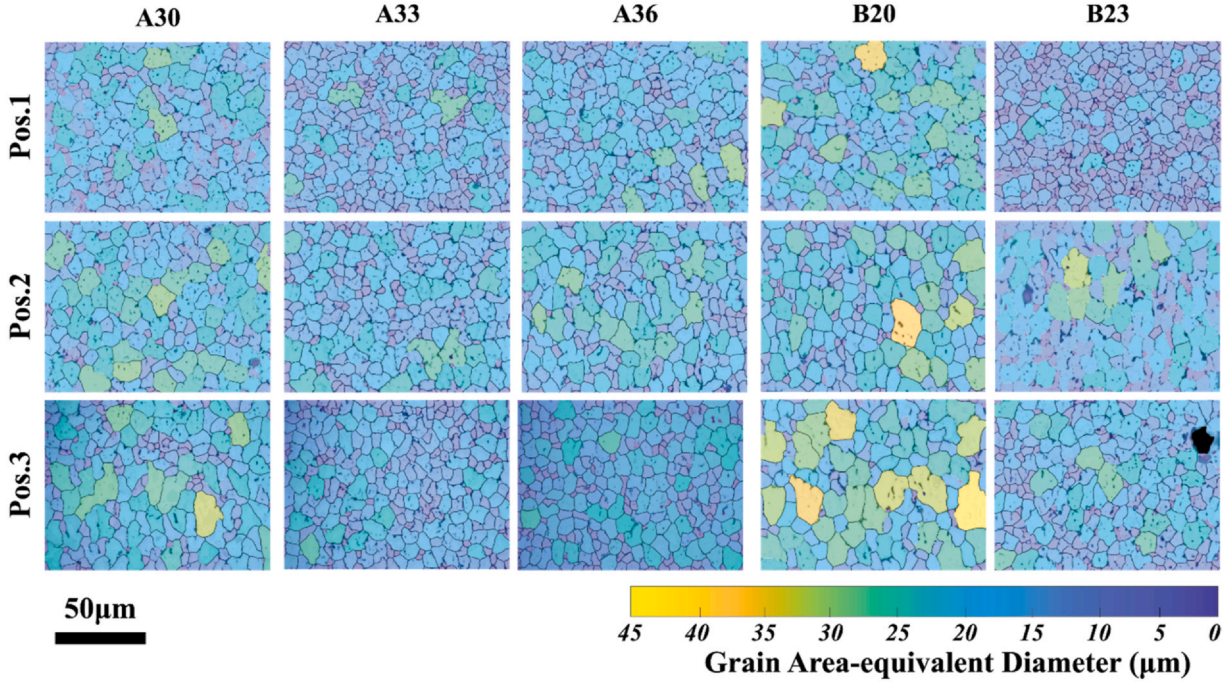

Fig. 7. Grain structure in position 1, 2, and 3 of all samples except B2X. Yellow color indicates larger grains while blue color represents finer grains.

relatively small molten pool size, which compromised the UA benefits. The UA effect in improving grain structure homogeneity was more significant at a lower welding speed, as in Group #B, which was achieved through a longer UA-melt interaction time.

Despite all the advantages, TiB_2 nanoparticles have the tendency to agglomerate during the solidification process [41]. As shown in Fig. 8, four main types of nanoparticle agglomerations were observed in this study. Composition of the agglomerations was

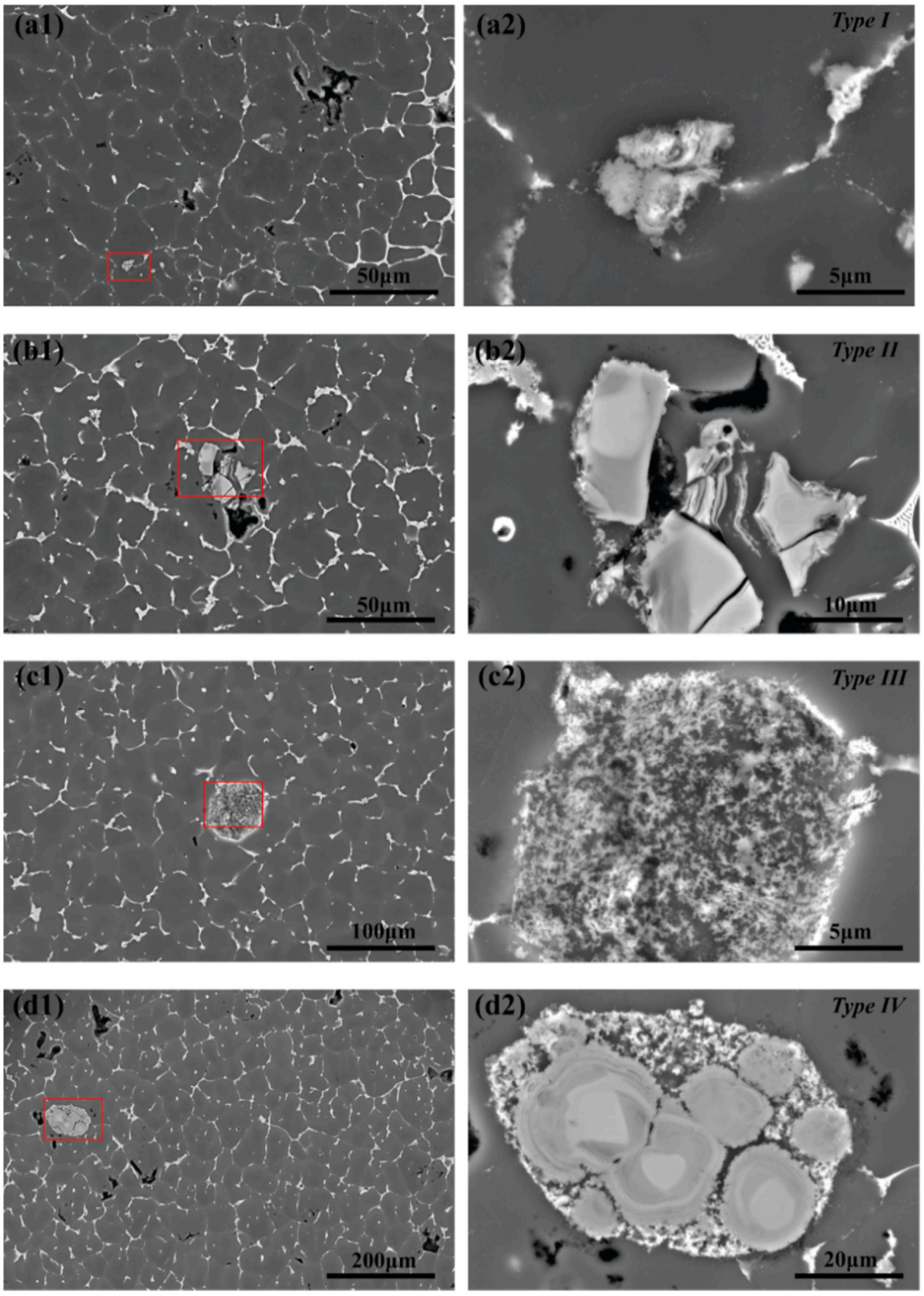

Fig. 8. Backscattered Electron (BSE) images of Type I cluster in (a1) and (a2), Type II cluster in (b1) and (b2), Type III cluster in (c1) and (c2), and Type IV cluster in (d1) and (d2). Clusters in (a1), (a2), (b1), and (b2) were observed in A33, and (c1), (c2), (d1), and (d2) showed clusters found in A30.

analyzed with Energy-dispersive X-ray spectroscopy (EDS). Elemental maps corresponding to type II, III and IV were presented in Fig. 9.

In the UA samples, clusters of nanoparticles with a size around 5 µm, denoted as Type I, were observed, as shown in Fig. 8 (a1 and a2). Similar size and morphology of the nanoparticle agglomerations were also observed in the previous UA-WAAM samples without the hot wire system [17]. Type I clusters can be observed both at grain boundaries and inside of the grains, indicating that they can be either pushed or engulfed by the solidification front [7,42]. Nanoparticles pushed by the solidification front can be trapped with the eutectic phases at the inter-dendritic region by the end of the solidification [43]. Fig. 8 (b1&b2) showed a cracked morphology of a dense Ti-rich plate next to a pore, which was denoted as Type II. Type II was also only observable in the UA samples. The corresponding EDS map in Fig. 9(a) showed only strong signal of Ti on the cracked plates whereas signals of Cu, Zn, and Mg were distributed in between, indicating formation of secondary phases surrounding the Type II agglomerations. Unlike the small Type I clusters, such agglomerations have a much larger size of ~30 µm. Type II agglomerations were only observed in the UA samples.

Fig. 8 (c1&c2) presented a large loose cluster of TiB_2 with a diameter of more than 50 µm, denoted as Type III cluster. This type of cluster showed a pseudo-spherical shape and was only observed in the no-UA conditions. EDS maps in Fig. 9(b) showed Ti distribution partially overlaps with Cu and Zn, indicating co-existing of secondary phase and nanoparticles in the same location. Signals of Mg and Al were detected in the lower region. Type IV agglomerations, as in Fig. 8 (d1&d2), were also only found in no-UA samples. This type of agglomeration contains several dense Ti-rich plates in the center surrounded by Type III clustering particles outside. The dense plates resemble the Type II agglomerations without the cracked morphology. EDS maps in Fig. 9(c) revealed that no strong signals of other alloying elements in addition to Ti were detected in the dense plate.

It can be hypothesized that Type II clusters are formed from Type IV clusters under ultrasonic vibration. The acoustic cavitation and streaming first disperse the loosely agglomerated nanoparticles at the outside boundary of Type IV clusters. The shock wave emitted from collapse of acoustic cavitation bubbles with enough intensities can then crack the Ti-rich plate in the center. It should be noted that the Ti-rich plates in Type II and IV are not common types of clusters in MMNC and are only occasionally observed in the build. They present in a morphology closer to sintering products. Since the melt pool temperature is generally lower than 1800 °C according to the measurement from infrared camera, these Ti-rich plates are not likely formed during solidification of the WAAM process. Instead, the Ti-rich plates were also observed in the weld wires, as shown in Fig. 10 (b), indicating that they can originate from the wire itself. Porosity was also noticed in the wire as shown in Fig. 10 (a), which was one of the sources of the hydrogen bubbles.

The sizes of type II, III and IV clusters are almost the same as those of the grains, which can have deleterious effects on the mechanical properties. The nanoparticle clusters are either surrounded or overlap with secondary phases, as they can serve as effective heterogeneous nucleating sites for secondary phase.

Fig. 11 compares the microstructure of the interlayer regions in B20 and B23 samples. In the no-UA B20 sample, the interlayer region is easily distinguishable with fewer secondary phases decorating the grain boundaries, as shown in Fig. 11 (a) and (b). This region is located below the fusion boundary and is formed due to the reheating from the following layer deposition, which dissolved the secondary phase back into the matrix. In the interlayer region, the grain size is generally larger, as observed in optical images in Fig. 6 and Fig. 7. This can be attributed to the grain growth from the reheating of following layers. As a comparison, in the UA B23 sample in Fig. 11 (c) and (d), the interlayer region is less distinguishable with either dissolution of secondary phase or grain coarsening.

Identifiable nanoparticle clusters were marked by red box in Fig. 11. More clusters can be noticed at the interlayer region. Besides, B20 contained more clusters and clusters with larger sizes than B23. According to the phase field modeling results by Y. Yang et al. [35] on nanoparticle distribution in a laser powder bed fusion process, the streamlines of melt flow frequently overlap and follow similar trajectories in the quasi-steady state condition. Besides, the nanoparticles at the melt pool bottom have low mobility. Accordingly, melt flow would drive nanoparticle clusters near the interlayer region. This explanation should also be applicable for GTAW-based WAAM process based on similarity.

The high intensity UA will induce cavitation and acoustic streaming effects. As discussed in 3.1, collapse of cavitation bubbles will release shockwaves, which facilitate ejection of possible clustered nanoparticles into the melts to improve the dispersion. The shockwaves can also break the Ti-rich plate, forming the cracked morphology of Type II in Fig. 8 (b2), compared to the bulk piece of Type IV in Fig. 8 (d2). Lastly, dendrites at the solid-liquid interface can be detached under the shockwaves, which was observed with in-situ synchrotron X-ray radiography during UA treatment of solidification of aluminum alloys [30]. Acoustic streaming will transport nanoparticles and detached dendrites into far end of the melt. The nanoparticles are further dispersed. Nanoparticles and detached dendrites can serve as heterogeneous nucleation sites during solidification.

3.5. UA enhanced mechanical properties

3.5.1. UA modified hardness and precipitation distribution

Fig. 12 shows the hardness distribution on the whole cross-sections in all the investigated deposit conditions. Except for the control test in B2X, all samples showed higher hardness than the baseline hardness of the weld wire, as provided in Fig. 10 (c). Low hardness bands were observed around the interlayer region in all samples, indicated by black box in Fig. 12. This corresponds to the dissolved secondary phases and larger grain size at the interlayer region, as shown in Fig. 11. The band is overall narrower and less distinguishable in the UA samples, which also agrees with the less distinguishable interlayer region in the microstructure (Fig. 11 (a&c)). The higher travel speed Group #A in general presented higher hardness than Group #B, which is based on fewer porosity, more refined grain structure, and less reheating effect with colder weld pool in the case of higher travel speed. All samples showed a middle-level hardness in the top beads, higher hardness in the middle beads, and lowest hardness in the bottom beads. This was consistent with the previous WAAM results without hot-wire system [17] and another WAAM study of the similar AA7075 wire enhanced with nanoparticles [44]. The inhomogeneity of hardness along the vertical building direction is caused by inherent different thermal cycles experienced at different heights during the multilayer deposition [45]. The top bead is in the as-deposit condition, where a minimal number of precipitates are formed due to the high cooling rate. The middle beads are subject to reheating when the top beads are deposited, which allows development of fine precipitates and

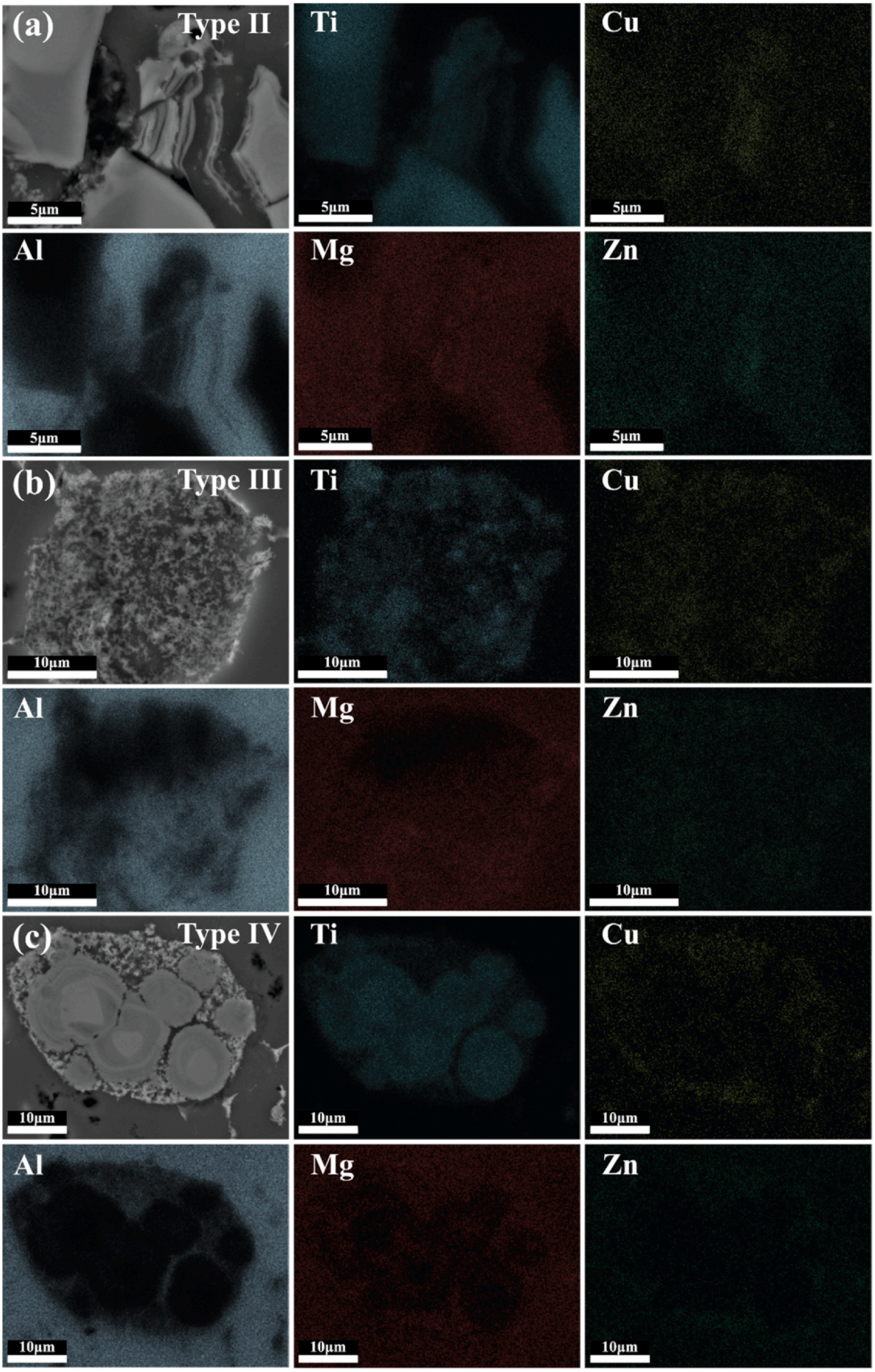

Fig. 9. Energy-dispersive X-ray spectroscopy (EDS) maps nanoparticle clusters (a) Type II in A33, (b) Type III in A30, and (c) Type IV in A30.

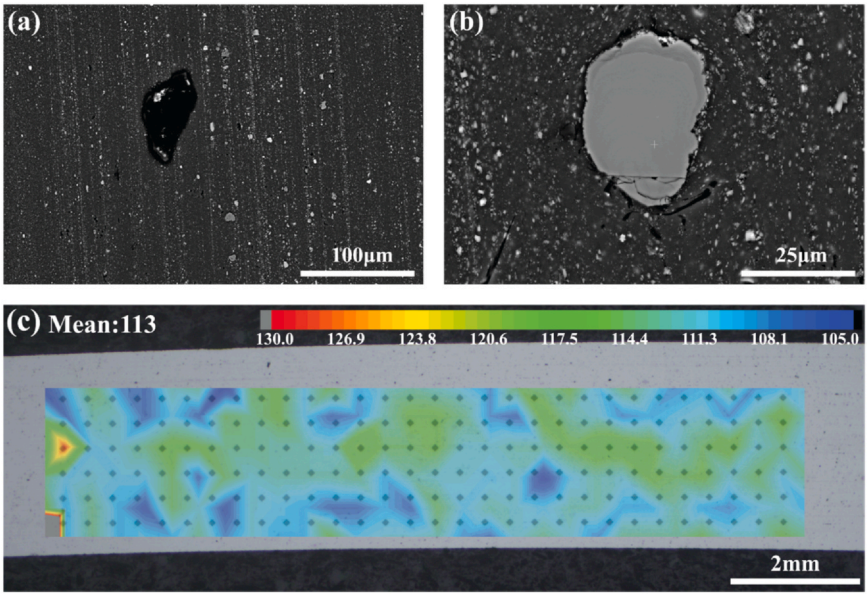

Fig. 10. BSE images of (a) porosity in the weld wire, (b) Type IV agglomeration in the weld wire, and (c) hardness distribution of the weld wire.

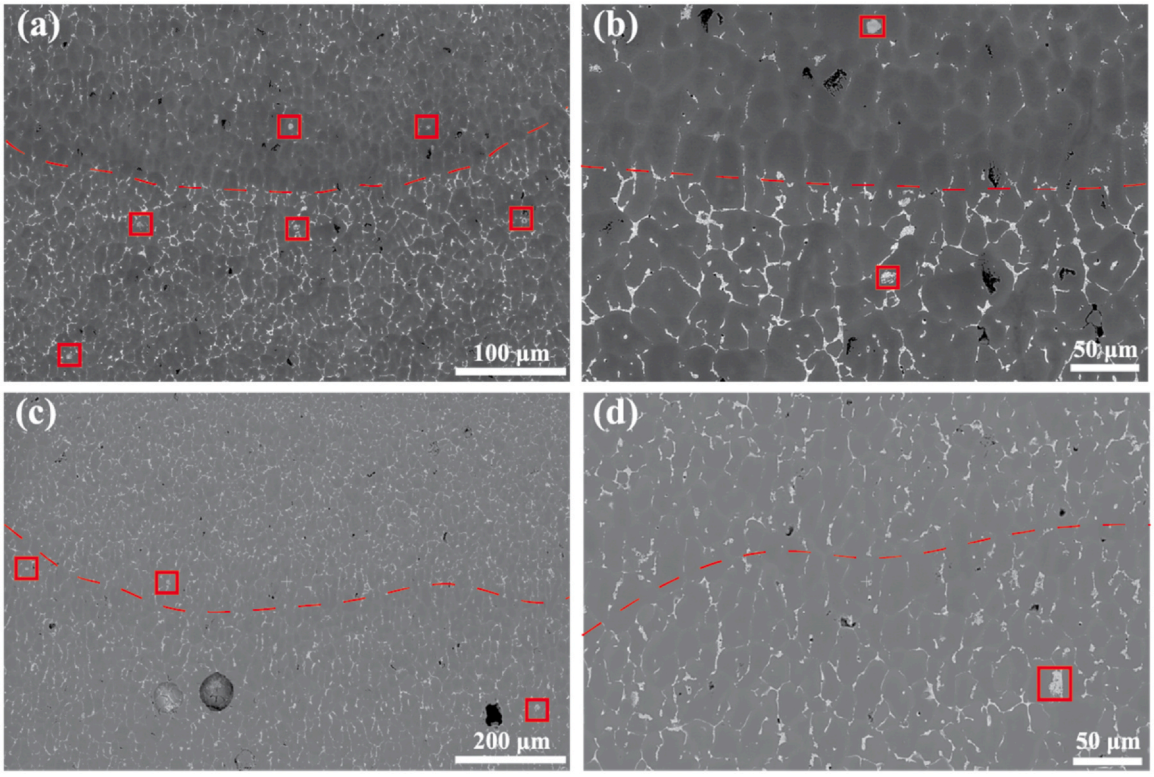

Fig. 11. BSE images of interlayer regions in (a)&(b) B20 and (c)&(d) B23. Agglomerations were indicated by red box. The red dashed lines indicate the isotherms where secondary phase is dissolved through reheating from the subsequent layers. The fusion boundaries should be above the red dashed lines.

resembles a peak-aged structure. The bottom beads will experience multiple thermal cycles, which lead to an over-aged structure with coarsened precipitates. Samples fabricated with UA and without UA showed comparable hardness distributions in the top and middle beads. On the other hand, in the bottom region, UA samples (A33, A36, B23) all showed higher hardness than the corresponding no-UA

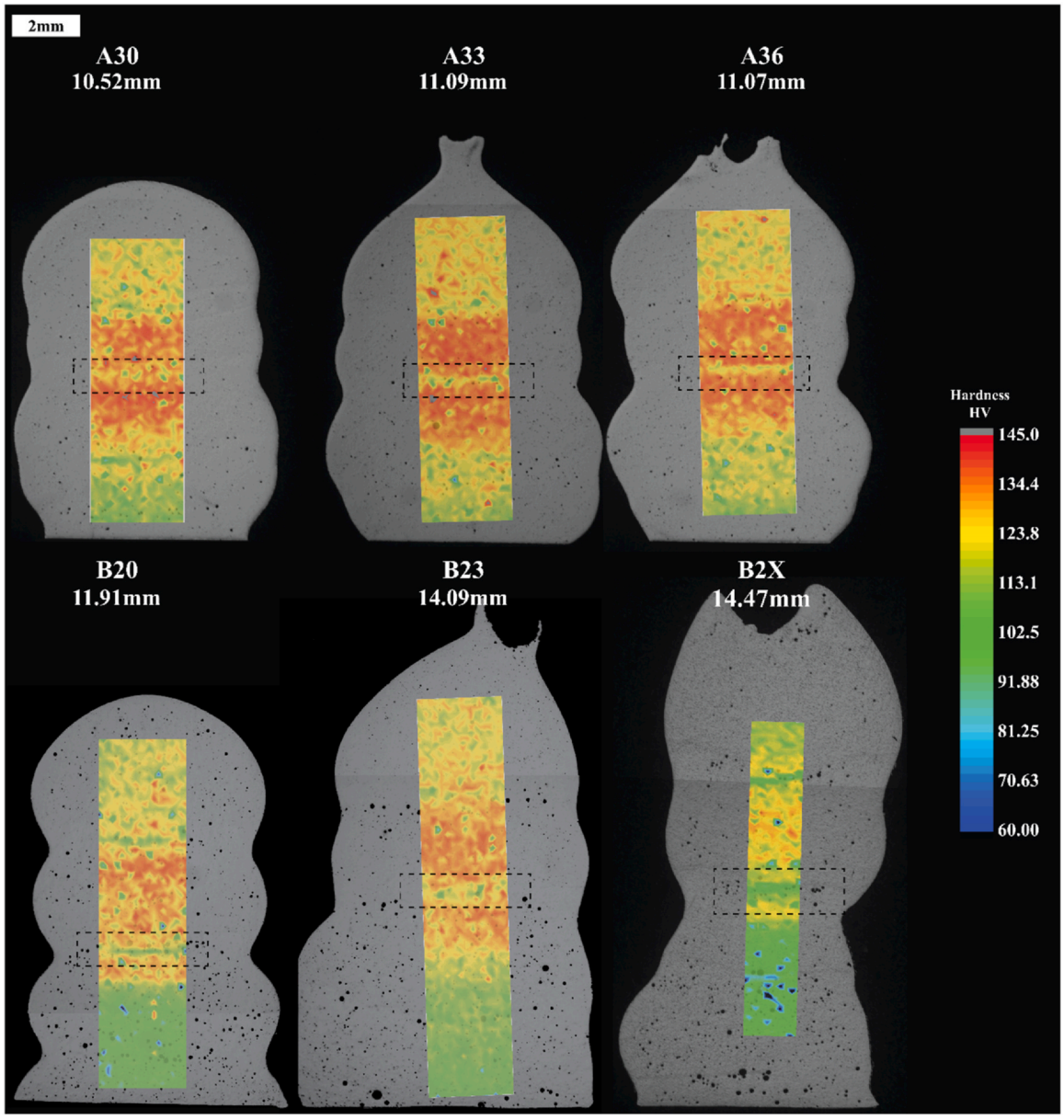

Fig. 12. Micro-hardness maps of all samples with lower hardness bands indicated by black boxes.

ones. Hardness distribution is more uniform throughout the building height in the UA sample, indicating a more homogenized microstructure.

The difference of hardness in the bottom beads between no-UA and UA samples can be directly related to the precipitation behavior. Fig. 13 (a & b) showed precipitate distribution near the grain boundary in the bottom beads of B20 while Fig. 13 (c & d) showed precipitate distribution at the same building height in B23. Clear precipitate free zones (PFZs) were observed near the grain boundaries. Close to PFZs, precipitates were generally finely distributed while coarsened ones were observed as moving towards the grain center, showing an over-aged microstructure in the no-UA condition. In contrast, fine precipitates were observed both in the grain center and near PFZ in the UA sample B23, which contributed to a higher hardness than the no-UA bottom region.

3.5.2. *Effect of UA on strength*

Fig. 14 shows the strength-elongation curves from micro-tensile tests for Group #B samples. 5 repeated tests were performed for B20 and B23 cases separately to account for the sample variations. In the UA condition (B23), an average tensile strength of 377.8 ± 40 MPa with elongation of 10.8 ± 1.45% was achieved. One sample in the UA group presented a very high tensile strength of 450 MPa. In comparison, the no-UA condition (B20) showed a lower average strength of 306.7 ± 46 MPa while the average elongation is slightly smaller than the UA result, as 9.8 ± 3.9%. Since the tensile specimen

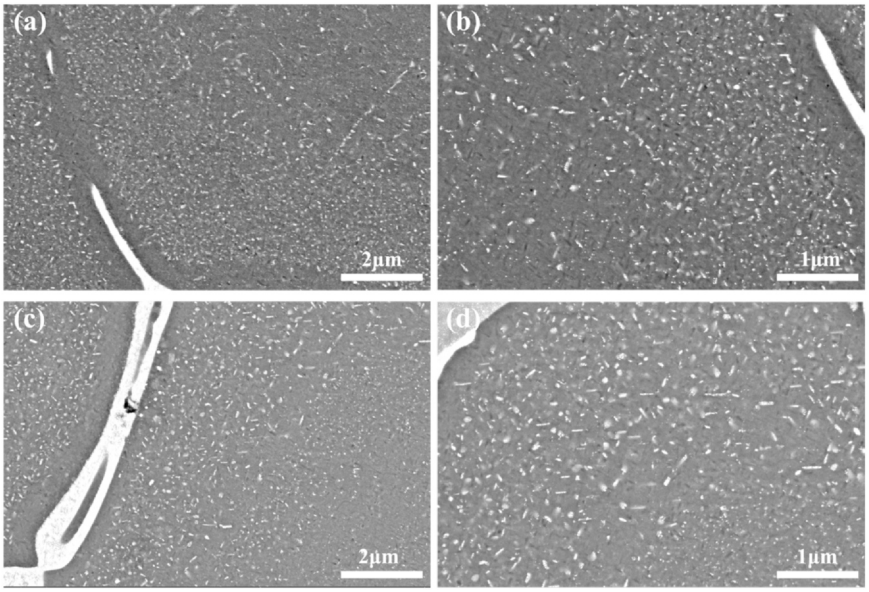

Fig. 13. BSE images of precipitates distribution at the bottom of (a & b) B20 and (c & d) B23.

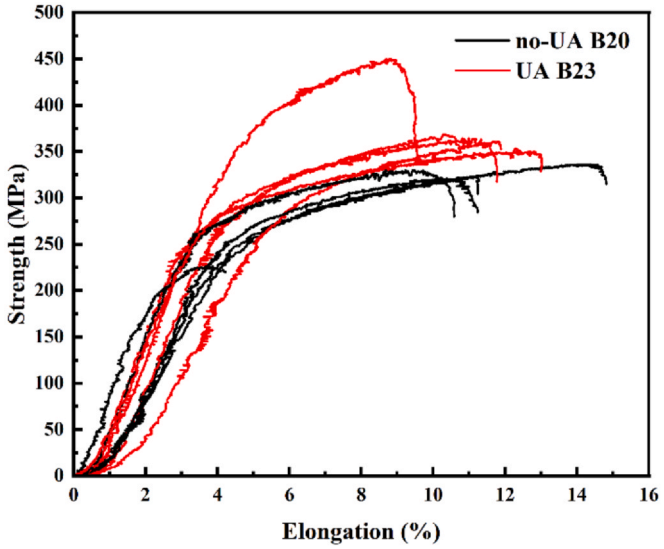

Fig. 14. Strength-elongation curve of micro-tensile tests of no-UA B20 and UA B23.

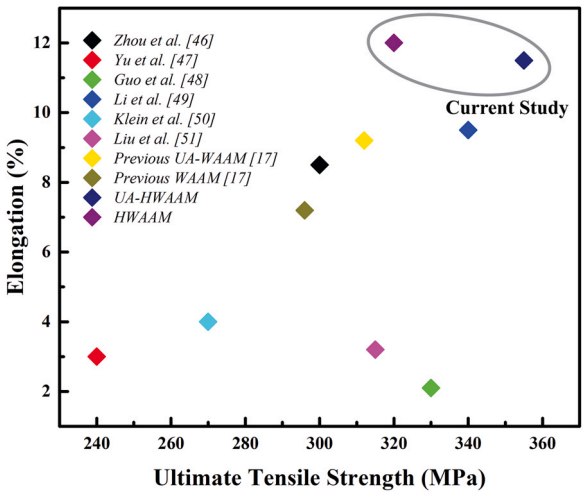

Fig. 15. Comparison of mechanical properties with previous studies of similar processes and materials.

included the interlayer region, where UA led to less dissolved secondary phase and more refined grains, the overall tensile strength was higher in the UA sample. One of the no-UA samples showed an early failure with a low tensile strength of 225 MPa and elongation of only 4.4%. As shown in the porosity analysis, the no-UA sample contained higher amount of porosity than UA one in the low travel speed #B group. Accordingly, the possibility of capturing porosity in the micro-tensile specimen was higher in the no-UA case, which led to an early failure. Comparing the mechanical properties in current studies with previous studies with similar materials and processes [17,46–51], 7075 MMNC fabricated by UA-HWAAM showed excellent tensile strength and elongation, as shown in Fig. 15.

Fig. 16 shows the strain distribution on the micro-tensile bars extracted at 2% and 4% elongation from DIC analysis. At 2% elongation, a strain concentration was already visible in the no-UA sample, indicated by the white box in Fig. 16 (a1). At higher 4% elongation, the strain concentration at this location becomes more significant, as shown in Fig. 16 (a2). Further fractography analysis revealed that porosities caused such early strain concentration. In contrast, strain concentration was not developed in the UA-sample until 4% strain, as shown in Fig. 16 (b2).

To further examine the failure behavior of micro-tensile test sample, fractographical analysis was performed, as shown in Fig. 17. A pore defect was observed at the fracture point near the gauge edge in the no-UA sample with the early failure, which corresponded with

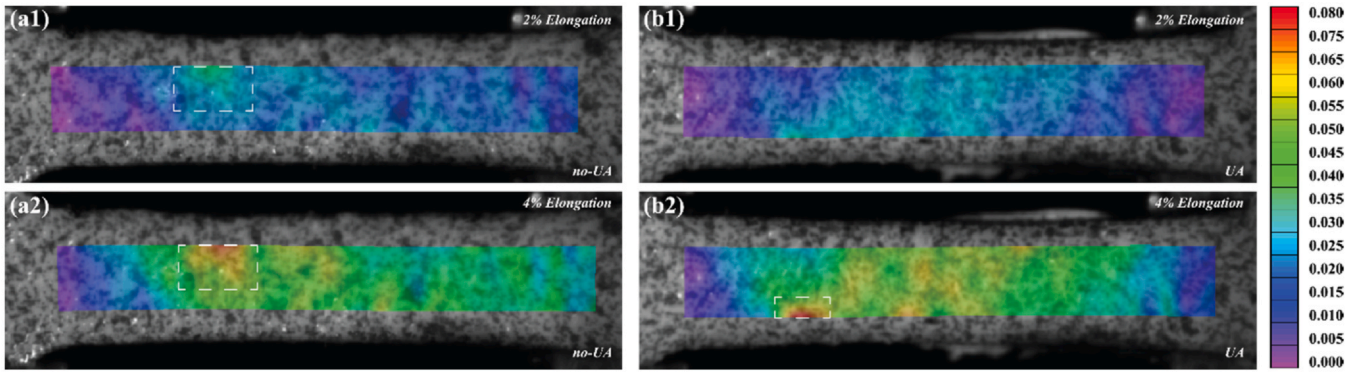

Fig. 16. DIC results during the tensile tests of no-UA sample at (a1) 2% elongation and (a2) 4% elongation; DIC results during the tensile tests of UA sample at (b1) 2% elongation and (b2) 4% elongation.

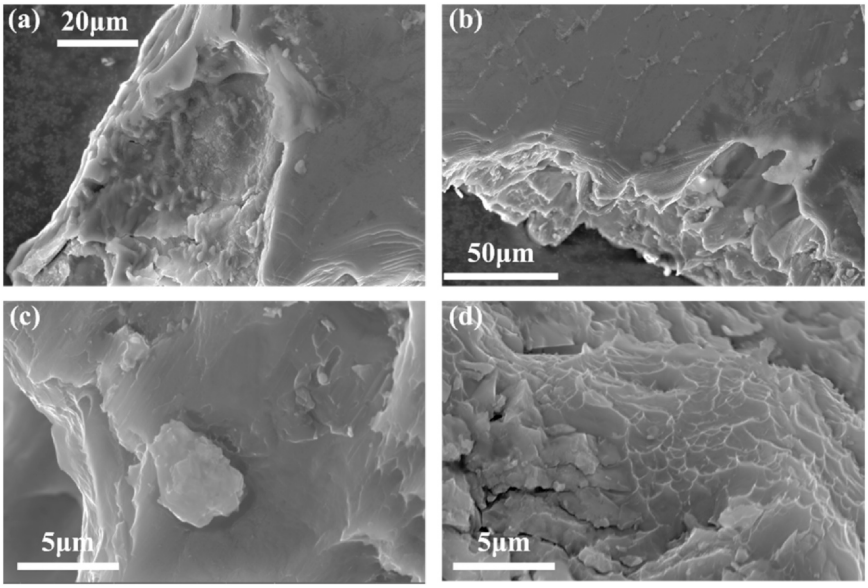

Fig. 17. Fractography analysis of micro-tensile bars:(a) porosity at the fracture in no-UA B20 sample with early failure, (b) top view of the fracture in no-UA B20, (c) fracture surface of no-UA B20 containing a nanoparticle cluster, and (d) fracture surface of UA B23.

the early strain concentration in the DIC analysis in Fig. 16 (a). Thus, the early failure could be ascribed to existence of porosity in the micro-tensile bar. Fig. 17 (b) provided an oblique view of the fracture surface of the same no-UA tested sample, where the main gauge surface could also be examined. This reveals that the fracture occurred in the interlayer region where lower hardness and dissolution of secondary phases was located. As shown in Fig. 17 (c), flat cleavage features were commonly noticed in fracture surfaces of no-UA samples. A nanoparticle cluster was also identified. Corresponding elemental mapping of this region was provided in Fig. 18. A strong signal of Ti was detected in the cluster, together with Mg, Zn, and Cu. The size of this cluster was around 5 μm, indicating it was likely to be the type I cluster co-located with secondary phases.

In the case of UA samples, more dimple-like ductile structures were found at the fracture surface. No large porosities or nanoparticle clusters were noticed. It is also difficult to locate the relative position of interlayer region and the fracture surface for the UA sample, since the interlayer region is less identifiable. This can also help with the uniform strain distribution during the deformation of UA sample, as shown in the DIC results.

The strengthening mechanisms of MMNC and the effect of UA on the hardening behavior were discussed in our previous study [17]. The strengthening of MMNC was contributed by the interaction of nano-sized reinforcements and dislocation, along with the strengthening effect from grain refinement. The UA promoted better dispersion of nanoparticles and more homogeneous microstructure, hence leveraged the enhancement of nanoparticles. Well-dispersed nanoparticles increased the dislocation density in the matrix and diminished the mobility of dislocations. Meanwhile, better dispersion of nanoparticles from UA enhanced the grain refining effect by providing more nucleation sites during the solidification process. Besides, it was reported that UA can greatly improve the wettability of particles in fabrication of metal matrix composites [14]. In a system of a MMNC, the contact angle between reinforcements and liquid melt dictates the wettability. During an UA melt treatment, the expansion phase will introduce an external force to enlarge the

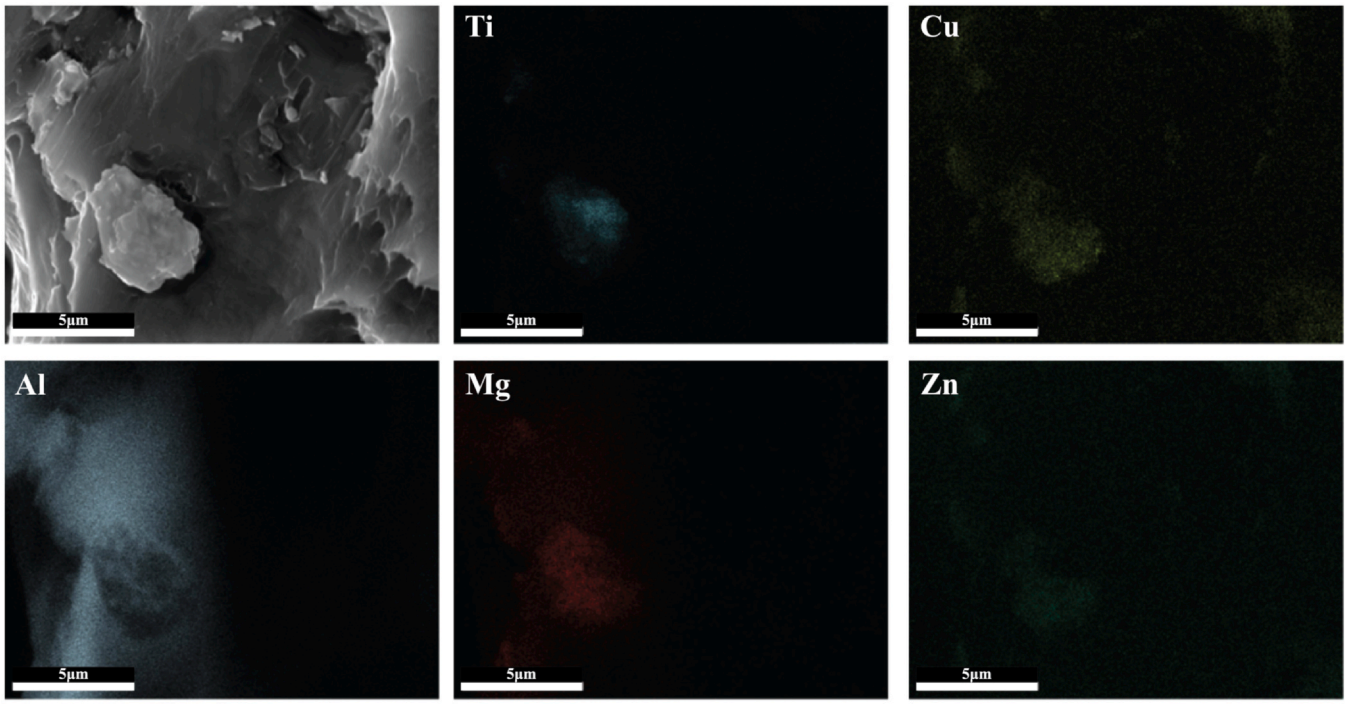

Fig. 18. Energy-dispersive X-ray spectroscopy (EDS) maps of fracture surface of B20 showing nanoparticle cluster.

surface of the droplet and therefore reduce the contact angle, therefore improve the wettability. The rarefaction phase will shrink the surface, but the contact angle hysteresis will keep the contact angle from increasing[52]. Thus, better wettability can be obtained under the UA treatment and hence promoted effective bonding between the nanoparticle and matrix. All these contributed to the improvements in mechanical properties.

4. Conclusion

The newly developed UA-HWAAM process for building TiB2 based AA7075 MMNC was thoroughly studied. Main conclusions are as the followings:

a) Hot-wire system can effectively reduce porosity during GTA-based WAAM process of nanoparticles. Higher travel speed would directly reduce the melt pool size and peak temperature, which reduces porosity and refines grain structure.UA on porosity reduction and grain refinement is more effective under low travel speed due to longer UA-melt interaction time. Higher UA intensity is not necessarily more beneficial in porosity and grain improvement.
b) Nanoparticle dispersion can be greatly improved by UA. Macroscopic nanoparticle agglomerations and Ti-rich plates identified in the no-UA samples are transformed to micro-sized clusters and cracked Ti-rich plates respectively in the UA-samples.
c) Higher tensile strength and more uniform strain distribution during the tensile tests is achieved in UA samples. Porosities and nanoparticle clusters are observed in fracture surface of the regular HWAAM sample, which correspond to inferior mechanical performance.
d) Under the UA effects, the interlayer region with dissolution of secondary phase and grain coarsening is less identifiable. Besides, over aging of precipitates at the bottom layers of deposition is less significant. Both these microstructure features lead to more uniform hardness distribution in the UA sample.

CRediT authorship contribution statement

Tianzhao Wang: Conceptualization, Methodology, Validation, Formal analysis, Writing – original draft, Writing – review & editing, Visualization, Data curation. **Jiarui Kang:** Methodology, Validation, Formal analysis. **Mason Darnell:** Formal analysis. **Xun Liu:** Conceptualization, Methodology, Writing – review & editing, Supervision, Project administration, Funding acquisition.

Data Availability

Data will be made available on request.

Declaration of Competing Interest

The authors declare that they have no known competing financial interests or personal relationships that could have appeared to influence the work reported in this paper.

Acknowledgement

This work was supported by National Science Foundation, United States, CMMI AM Award # 2044526: CAREER: Ultrasonically Assisted Wire Arc Additive Manufacturing of Metal Matrix Nanocomposites for High-strength, Lightweight Structures. Electron microscopy was performed at the Center for Electron Microscopy and Analysis (CEMAS) at The Ohio State University.

References

[1] L. Ceschini, A. Dahle, M. Gupta, A.E.W. Jarfors, S. Jayalakshmi, A. Morri, F. Rotundo, S. Toschi, R.A. Singh, Aluminum and Magnesium Metal Matrix Nanocomposites, Springer, Singapore, Singapore, 2017, https://doi.org/10.1007/978-981-10-2681-2
[2] M. Sokoluk, C. Cao, S. Pan, X. Li, Nanoparticle-enabled phase control for arc welding of unweldable aluminum alloy 7075, Nat. Commun. 10 (2019) 98, https://doi.org/10.1038/s41467-018-07989-y

[3] T.-C. Lin, C. Cao, M. Sokoluk, L. Jiang, X. Wang, J.M. Schoenung, E.J. Lavernia, X. Li, Aluminum with dispersed nanoparticles by laser additive manufacturing, Nat. Commun. 10 (2019) 4124, https://doi.org/10.1038/s41467-019-12047-2
[4] R. Casati, M. Vedani, Metal matrix composites reinforced by nano-particles—a review, Metals 4 (2014) 65–83, https://doi.org/10.3390/met4010065
[5] S. Amirkhanlou, M. Ketabchi, N. Parvin, A. Orozco-Caballero, F. Carreño, Homogeneous and ultrafine-grained metal matrix nanocomposite achieved by accumulative press bonding as a novel severe plastic deformation process, Scr. Mater. 100 (2015) 40–43, https://doi.org/10.1016/j.scriptamat.2014.12.007
[6] M. Sokoluk, J. Yuan, S. Pan, X. Li, Nanoparticles enabled mechanism for hot cracking elimination in aluminum alloys, Met. Mater. Trans. A 52 (2021) 3083–3096, https://doi.org/10.1007/s11661-021-06302-9
[7] J. Wu, Z. Zhou, M. Ma, Z. Zhang, G. Chen, Y. Zhao, J. Pi, Serrated flow and ZrB2 nanoparticle agglomerations of in-situ AA6061 alloy matrix composites, J. Alloy. Compd. 846 (2020) 156476, https://doi.org/10.1016/j.jallcom.2020.156476
[8] D.J. Lloyd, Particle reinforced aluminium and magnesium matrix composites, Int. Mater. Rev. 39 (1994) 1–23, https://doi.org/10.1179/imr.1994.39.1.1
[9] G.I. Eskin, Cavitation mechanism of ultrasonic melt degassing, Ultrason. Sonochem. 2 (1995) S137–S141, https://doi.org/10.1016/1350-4177(95)00020-7
[10] G.I. Eskin, D.G. Eskin, Ultrasonic Treatment Of Light Alloy Melts, CRC press, 2014.
[11] W. Mirihanage, W. Xu, J. Tamayo-Ariztondo, D. Eskin, M. Garcia-Fernandez, P. Srirangam, P. Lee, Synchrotron radiographic studies of ultrasonic melt processing of metal matrix nano composites, Mater. Lett. 164 (2016) 484–487, https://doi.org/10.1016/j.matlet.2015.11.022
[12] C.R. Cunningham, J.M. Flynn, A. Shokrani, V. Dhokia, S.T. Newman, Invited review article: strategies and processes for high quality wire arc additive manufacturing, Addit. Manuf. 22 (2018) 672–686, https://doi.org/10.1016/j.addma.2018.06.020
[13] H. Xu, Q. Han, T.T. Meek, Effects of ultrasonic vibration on degassing of aluminum alloys, Mater. Sci. Eng.: A 473 (2008) 96–104, https://doi.org/10.1016/j.msea.2007.04.040
[14] X. Li, Y. Yang, X. Cheng, Ultrasonic-assisted fabrication of metal matrix nanocomposites, J. Mater. Sci. 39 (2004) 3211–3212, https://doi.org/10.1023/B:JMSC.0000025862.23609.6f
[15] H. Ye, K. Ye, B. Guo, F. Le, C. Wei, X. Sun, G. Wang, Y. Liu, Effects of combining ultrasonic micro-forging treatment with laser metal wire deposition on microstructural and mechanical properties in Ti–6Al–4V alloy, Mater. Charact. 162 (2020) 110187, https://doi.org/10.1016/j.matchar.2020.110187
[16] C.J. Todaro, M.A. Easton, D. Qiu, D. Zhang, M.J. Bermingham, E.W. Lui, M. Brandt, D.H. StJohn, M. Qian, Grain structure control during metal 3D printing by high-intensity ultrasound, Nat. Commun. 11 (2020) 142, https://doi.org/10.1038/s41467-019-13874-z
[17] T. Wang, V. Mazánová, X. Liu, Ultrasonic effects on gas tungsten arc based wire additive manufacturing of aluminum matrix nanocomposite, Mater. Des. 214 (2022) 110393, https://doi.org/10.1016/j.matdes.2022.110393
[18] Z. Nie, G. Wang, J.D. McGuffin-Cawley, B. Narayanan, S. Zhang, D. Schwam, M. Kottman, Y. (Kevin) Rong, Experimental study and modeling of H13 steel deposition using laser hot-wire additive manufacturing, J. Mater. Process. Technol. 235 (2016) 171–186, https://doi.org/10.1016/j.jmatprotec.2016.04.006
[19] R. Fu, S. Tang, J. Lu, Y. Cui, Z. Li, H. Zhang, T. Xu, Z. Chen, C. Liu, Hot-wire arc additive manufacturing of aluminum alloy with reduced porosity and high deposition rate, Mater. Des. 199 (2021) 109370, https://doi.org/10.1016/j.matdes.2020.109370
[20] S. Suresh, N. Shenbag, V. Moorthi, Aluminium-titanium diboride (Al-TiB2) metal matrix composites: challenges and opportunities, Procedia Eng. 38 (2012) 89–97, https://doi.org/10.1016/j.proeng.2012.06.013
[21] R.W. Niles, C. Jackson, Weld thermal efficiency of the GTAW process, Weld. J. 54 (1975) 25.
[22] K.-D. Li, E. Chang, Mechanism of nucleation and growth of hydrogen porosity in solidifying A356 aluminum alloy: an analytical solution, Acta Mater. 52 (2004) 219–231, https://doi.org/10.1016/j.actamat.2003.09.007
[23] D.R. Poirier, K. Yeum, A.L. Maples, A thermodynamic prediction for microporosity formation in aluminum-rich Al-Cu alloys, MTA 18 (1987) 1979–1987, https://doi.org/10.1007/BF02647028
[24] L.M. Siqveland, S.M. Skjaeveland, Derivations of the Young-Laplace equation, Capillarity 4 (2021) 23–30, https://doi.org/10.46690/capi.2021.02.01
[25] J.P. Anson, R.A.L. Drew, J.E. Gruzleski, The surface tension of molten aluminum and Al-Si-Mg alloy under vacuum and hydrogen atmospheres, Met. Mater. Trans. B 30 (1999) 1027–1032, https://doi.org/10.1007/s11663-999-0108-4
[26] W.A. Tiller, K.A. Jackson, J.W. Rutter, B. Chalmers, The redistribution of solute atoms during the solidification of metals, Acta Metall. 1 (1953) 428–437, https://doi.org/10.1016/0001-6160(53)90126-6
[27] D.E.J. Talbot, P.N. Anyalebechi, Solubility of hydrogen in liquid aluminium, Mater. Sci. Technol. 4 (1988) 1–4, https://doi.org/10.1179/mst.1988.4.1.1
[28] X. Meng, G. Qin, Z. Zou, Sensitivity of driving forces on molten pool behavior and defect formation in high-speed gas tungsten arc welding, Int. J. Heat. Mass Transf. 107 (2017) 1119–1128, https://doi.org/10.1016/j.ijheatmasstransfer.2016.11.025
[29] W.-I. Cho, S.-J. Na, Impact of driving forces on molten pool in gas metal arc welding, Weld. World 65 (2021) 1735–1747, https://doi.org/10.1007/s40194-021-01138-8
[30] F. Wang, D. Eskin, J. Mi, C. Wang, B. Koe, A. King, C. Reinhard, T. Connolley, A synchrotron X-radiography study of the fragmentation and refinement of primary intermetallic particles in an Al-35 Cu alloy induced by ultrasonic melt processing, Acta Mater. 141 (2017) 142–153, https://doi.org/10.1016/j.actamat.2017.09.010
[31] E. Scheil, Bemerkungen zur Schichtkristallbildung, Int. J. Mater. Res. 34 (1942) 70–72, https://doi.org/10.1515/ijmr-1942-340303
[32] C.J. Farnin, J.M. Rickman, J.N. DuPont, Solutions to the scheil equation with a variable partition coefficient, Met. Mater. Trans. A 52 (2021) 5443–5448, https://doi.org/10.1007/s11661-021-06482-4
[33] K. Yasui, Acoustic Cavitation and Bubble Dynamics, Springer International Publishing, Cham, 2018, https://doi.org/10.1007/978-3-319-68237-2
[34] M. Yang, Z. Yang, B. Cong, B. Qi, How ultra high frequency of pulsed gas tungsten arc welding affects weld porosity of Ti-6Al-4V alloy, Int J. Adv. Manuf. Technol. 76 (2015) 955–960, https://doi.org/10.1007/s00170-014-6324-3
[35] Y. Yang, C. Doñate-Buendía, T.D. Oyedeji, B. Gökce, B.-X. Xu, Nanopart. Tracing Laser Powder Bed Fusion Oxide Dispers. Strength. Steels (2021) 24.
[36] M.J. Assael, K. Kakosimos, R.M. Banish, Reference data for the density and viscosity of liquid aluminum and liquid iron, J. Phys. Chem. Ref. Data. 35 (2006) 17.
[37] A. Horgar, H. Fostervoll, B. Nyhus, X. Ren, M. Eriksson, O.M. Akselsen, Additive manufacturing using WAAM with AA5183 wire, J. Mater. Process. Technol. 259 (2018) 68–74, https://doi.org/10.1016/j.jmatprotec.2018.04.014
[38] E.M. Ryan, T.J. Sabin, J.F. Watts, M.J. Whiting, The influence of build parameters and wire batch on porosity of wire and arc additive manufactured aluminium alloy 2319, J. Mater. Process. Technol. 262 (2018) 577–584, https://doi.org/10.1016/j.jmatprotec.2018.07.030
[39] B. Cong, J. Ding, S. Williams, Effect of arc mode in cold metal transfer process on porosity of additively manufactured Al-6.3%Cu alloy, Int J. Adv. Manuf. Technol. 76 (2015) 1593–1606, https://doi.org/10.1007/s00170-014-6346-x
[40] W. Stopyra, K. Gruber, I. Smolina, T. Kurzynowski, B. Kuznicka, Laser powder bed fusion of AA7075 alloy_ Influence of process parameters on porosity and hot cracking, Addit. Manuf. (2020) 15.
[41] A.R. Kennedy, A.E. Karantzalis, S.M. Wyatt, The microstructure and mechanical properties of TiC and TiB2-reinforced cast metal matrix composites, (n.d.) 8.
[42] J.K. Kim, P.K. Rohatgi, An analytical solution of the critical interface velocity for the encapturing of insoluble particles by a moving solid/liquid interface, Met. Mat. Trans. A 29 (1998) 351–358, https://doi.org/10.1007/s11661-998-0186-y
[43] J.Q. Xu, L.Y. Chen, H. Choi, X.C. Li, Theoretical study and pathways for nanoparticle capture during solidification of metal melt, J. Phys.: Condens. Matter 24 (2012) 255304, https://doi.org/10.1088/0953-8984/24/25/255304
[44] D. Oropeza, D.C. Hofmann, K. Williams, S. Firdosy, P. Bordeenithikasem, M. Sokoluk, M. Liese, J. Liu, X. Li, Welding and additive manufacturing with nanoparticle-enhanced aluminum 7075 wire, J. Alloy. Compd. 834 (2020) 154987, https://doi.org/10.1016/j.jallcom.2020.154987
[45] V.A. Hosseini, M. Högström, K. Hurtig, M.A. Valiente Bermejo, L.-E. Stridh, L. Karlsson, Wire-arc additive manufacturing of a duplex stainless steel: thermal cycle analysis and microstructure characterization, Weld. World 63 (2019) 975–987, https://doi.org/10.1007/s40194-019-00735-y
[46] Y. Zhou, X. Lin, N. Kang, W. Huang, J. Wang, Z. Wang, Influence of travel speed on microstructure and mechanical properties of wire + arc additively manufactured 2219 aluminum alloy, J. Mater. Sci. Technol. 37 (2020) 143–153, https://doi.org/10.1016/j.jmst.2019.06.016
[47] Z. Yu, T. Yuan, M. Xu, H. Zhang, X. Jiang, S. Chen, Microstructure and mechanical properties of Al-Zn-Mg-Cu alloy fabricated by wire + arc additive manufacturing, J. Manuf. Process. 62 (2021) 430–439, https://doi.org/10.1016/j.jmapro.2020.12.045
[48] X. Guo, H. Li, Z. Pan, S. Zhou, Microstructure and mechanical properties of ultra-high strength Al-Zn-Mg-Cu-Sc aluminum alloy fabricated by wire + arc additive manufacturing, J. Manuf. Process. 79 (2022) 576–586, https://doi.org/10.1016/j.jmapro.2022.05.009
[49] S. Li, L.-J. Zhang, J. Ning, X. Wang, G.-F. Zhang, J.-X. Zhang, S.-J. Na, Microstructures and mechanical properties of Al–Zn–Mg aluminium alloy samples produced by wire + arc additive manufacturing, J. Mater. Res. Technol. 9 (2020) 13770–13780, https://doi.org/10.1016/j.jmrt.2020.09.114
[50] T. Klein, M. Schnall, B. Gomes, P. Warczok, D. Fleischhacker, P.J. Morais, Wire-arc additive manufacturing of a novel high-performance Al-Zn-Mg-Cu alloy: processing, characterization and feasibility demonstration, Addit. Manuf. 37 (2021) 101663, https://doi.org/10.1016/j.addma.2020.101663
[51] D. Liu, D. Wu, R. Wang, J. Shi, F. Niu, G. Ma, Formation mechanism of Al-Zn-Mg-Cu alloy fabricated by laser-arc hybrid additive manufacturing: microstructure evaluation and mechanical properties, Addit. Manuf. 50 (2022) 102554, https://doi.org/10.1016/j.addma.2021.102554
[52] J.A. Sarasua, L.R. Rubio, E. Aranzabe, J.L.V. Vilela, Energetic study of ultrasonic wettability enhancement, Ultrason. Sonochem. 79 (2021) 105768, https://doi.org/10.1016/j.ultsonch.2021.105768